Materials Research Letters

ISSN: (Print) 2166-3831 (Online) Journal homepage: https://www.tandfonline.com/loi/tmrl20

# $SrTiO_3$ termination control: a method to tailor the oxygen exchange kinetics

Felix V. E. Hensling, Christoph Baeumer, Marc-André Rose, Felix Gunkel & Regina Dittmann

**To cite this article:** Felix V. E. Hensling, Christoph Baeumer, Marc-André Rose, Felix Gunkel & Regina Dittmann (2020) $SrTiO_3$ termination control: a method to tailor the oxygen exchange kinetics, Materials Research Letters, 8:1, 31-40, DOI: 10.1080/21663831.2019.1682705

**To link to this article:** https://doi.org/10.1080/21663831.2019.1682705

MATER. RES. LETT.
2020, VOL. 8, NO. 1, 31–40
https://doi.org/10.1080/21663831.2019.1682705

MATERIALS RESEARCH LETTERS
Taylor & Francis
Taylor & Francis Group

ORIGINAL REPORT



# $SrTiO_3$ termination control: a method to tailor the oxygen exchange kinetics

Felix V. E. Hensling [a], Christoph Baeumer[a], Marc-André Rose[b], Felix Gunkel[a,b] and Regina Dittmann[a]

[a]Peter Grünberg Institut 7 & JARA-FIT, Forschungszentrum Jülich, Jülich, Germany; [b]Institute of Electronic Materials (IWE2) & JARA-FIT, RWTH Aachen University, Aachen, Germany

**ABSTRACT**

We provide insights into the influence of surface termination on the oxygen vacancy incorporation for the perovskite model material $SrTiO_3$ during annealing in reducing gas environments. We present a novel approach to tailor the oxygen vacancy formation by controlling the termination. We prove that a SrO-termination can inhibit the incorporation of oxygen vacancies across the (100)-surface and apply this to control their incorporation during thin film growth. Utilizing the conducting interface between $LaAlO_3$ and $SrTiO_3$, we could tailor the oxygen-vacancy based conductivity contribution by the level of SrO termination at the interface.

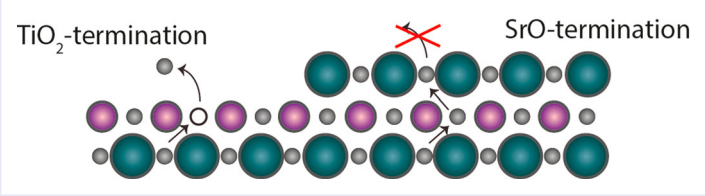


**IMPACT STATEMENT**

Termination dependent oxygen exchange is reported for the perovskite model material $SrTiO_3$ and used to improve the understanding and engineering of the 2D electron gas model system $LaAlO_3/SrTiO_3$.

**ARTICLE HISTORY**
Received 19 February 2019

**KEYWORDS**
Surface kinetics; 2DEGs; defect chemistry; substrate termination; oxide interfaces

## 1. Introduction

Transition metal oxides have become a central topic in research over the past decade due to their manifold interesting properties [1,2]. One of the most commonly used perovskites is $SrTiO_3$ (STO), which offers the advantage of a well-known defect chemistry. Typical applications for STO as a functional material are resistive switching devices [3], catalysis [4] or thermoelectrics [5].

Regardless of the application, the oxidation state of STO is a key parameter. In the field of thermoelectrics, oxygen vacancies are used to tailor the thermal conductivity of STO [5,6]. When using STO for (photo-)catalysis, specific doping with oxygen vacancies is utilized to increase the activity [7,8]. Resistive switching of STO is based on the generation and redistribution of oxygen vacancies. Thus oxygen vacancies generated during growth or dedicated annealing steps define its switching properties [9,10].

The central role of oxygen vacancies for all STO applications has resulted in intense research efforts to understand and control their formation [11–22]. Apart from the classic influence factors temperature and pressure [19–21], it was found that e.g. UV radiation [12,23–27] plays a crucial role. STO substrates are easily reduced during thin film growth at low oxygen pressure. This is a drawback as it can mask the functional properties of the deposited thin film. Although a strong termination dependence of the oxygen exchange kinetics has been demonstrated for other perovskites [28–30], it has only been scarcely considered for STO(100) [21,31,32], which can exhibit a $TiO_2$-termination, a SrO-termination or a mixed termination [33,34]. The termination of STO especially plays a key role for applications, which rely on interfaces. Examples are the properties of magnetic heterojunctions [35], interface dependent superconductivity [36], and the formation of a two-dimensional electron gas

**CONTACT** Felix V. E. Hensling felix.hensling@rwth-aachen.de Peter Grünberg Institut 7 & JARA-FIT, Forschungszentrum Jülich, 52425 Jülich, Germany

Supplemental data for this article can be accessed here. https://doi.org/10.1080/21663831.2019.1682705

(2DEG), as observed at the interface of the model system $LaAlO_3$(LAO)/STO [37–45]. The latter one is an outstanding candidate for an all-oxide field effect transistor [46–52].

Both properties, termination and oxidation state, thus play a central role in the field of STO applications. Yet their interplay has not been investigated so far, which is especially surprising as an influence of the termination layer on the oxygen exchange kinetics is well known for other perovskite systems. In this work, we will thoroughly investigate the role of the STO termination on the oxygen exchange kinetics. We find that the $TiO_2$-termination is more favorable to form oxygen vacancies, while the SrO-termination can completely suppress their formation. Hence, we present a new method to tailor the oxygen vacancy formation in $SrTiO_3$, namely by a precise control of the termination. In the course of this, we will present evidence for an instability of the SrO termination under ambient conditions. Finally, we will apply this knowledge to LAO/STO and show that we can tailor the resistivity of both, the crystalline system grown under reducing conditions and the amorphous system. As the resistivity for both systems depends on oxygen vacancies, we thus prove termination control is a new method for controlling the formation of oxygen vacancies.

## 2. Experimental

To systematically control different degrees of SrO-termination, SrO was deposited on $TiO_2$-terminated STO (treatment with buffered HF) [33,34] from a $SrO_2$ target with a laser fluence of 0.81 J/cm$^2$ utilizing a *Compex 205F -- COHERENT* 248 nm excimer laser at an oxygen pressure of $10^{-7}$ mbar and 800°C substrate temperature with a target substrate distance of 44 mm. The SrO coverage was controlled using the secondary spots of the reflective high energy electron diffraction pattern, which correspond to a SrO termination due to the higher atom form factor of Sr (supplementary Figure 1(a))[53,54]. The deposition of both, crystalline and amorphous LAO, was performed at the same target substrate distance, at $10^{-4}$ mbar and with a laser fluence of 1.3 J/cm$^2$ from a single crystalline LAO target. Amorphous LAO was grown at room temperature and crystalline LAO at 800°C with subsequent quenching (cool down time to below 400°C was about 40 s). The crystalline thin films were 8 unit cells thick, the amorphous about 12 unit cells.

For the *in situ* annealing process samples were annealed under oxidizing conditions after termination to minimize adsorbates. Subsequently, the annealing experiment was performed for 1 h at an oxygen pressure of $10^{-6}$ mbar at 800°C with subsequent quenching (cool down time to below 400°C was about 40 s).

The *ex situ* samples were stored at room temperature under ambient conditions for 60 h before being exposed to the same annealing conditions.

Electrical characterization at room temperature was performed using a *Lakeshore 8400 Series* Hall measurement setup. Low-temperature electrical characterization was performed with a physical property measurement setup. The XPS is a *PHI 5000 Versa Probe* and the AFM a *Omicron VT AFM XA*. The photoemission angle was 45° and the spectra were fitted using *Casa XPS* with a Shirley background and a convolution of Gaussian and Lorentzian line shape.

## 3. Results

### 3.1. Interplay of termination and oxygen vacancy incorporation

In order to investigate the termination dependent oxygen vacancy incorporation, STO single crystals were SrO- and $TiO_2$-terminated selectively. The resulting topographies are shown in Figure 1. Figure 1(a) shows an atomically flat $TiO_2$ terminated sample and Figure 1(b) shows a sample with 50% of SrO termination, resulting in an island type coverage. Figure 1(e) shows a SrO terminated sample. The successful SrO termination is underlined by the conserved STO step height (supplementary Figure 1(b,c)). We further utilize XPS measurements to confirm the successful termination of the respective samples. Comparing the Sr 3d spectra (supplementary Figure 2(a)) and the Ti 2p spectra (supplementary Figure 2(b)) we find 54% Sr/(Sr+Ti) and 46% Ti/(Sr+Ti) for a SrO termination and 48% Sr/(Sr+Ti) and 52% Ti/(Sr+Ti) for a $TiO_2$ termination, respectively. These values are in good agreement with our previously published work [55].

After termination, we applied the *in situ* annealing process at $10^{-6}$ mbar and 800°C. The subsequent quenching of the samples preserves the defect equilibrium achieved at high temperatures. Figure 1(c) shows the resulting carrier concentration $n$, which is a measure for the oxygen vacancy concentration, for $TiO_2$ and SrO terminated STO (red square). The resulting carrier concentration for the $TiO_2$ terminated sample is $5 \times 10^{18}$ cm$^{-3}$, a typical value observed for the applied conditions [11,56]. The carrier concentration of the SrO terminated sample after the same treatment is, however, below the measurement limit ($< 10^{10}$ cm$^{-3}$). This is a first hint to a termination dependency of the oxygen vacancy formation.

The observed behavior, however, changes drastically after SrO terminated STO was exposed to ambient conditions for 60 h. The annealing of *ex situ* samples results

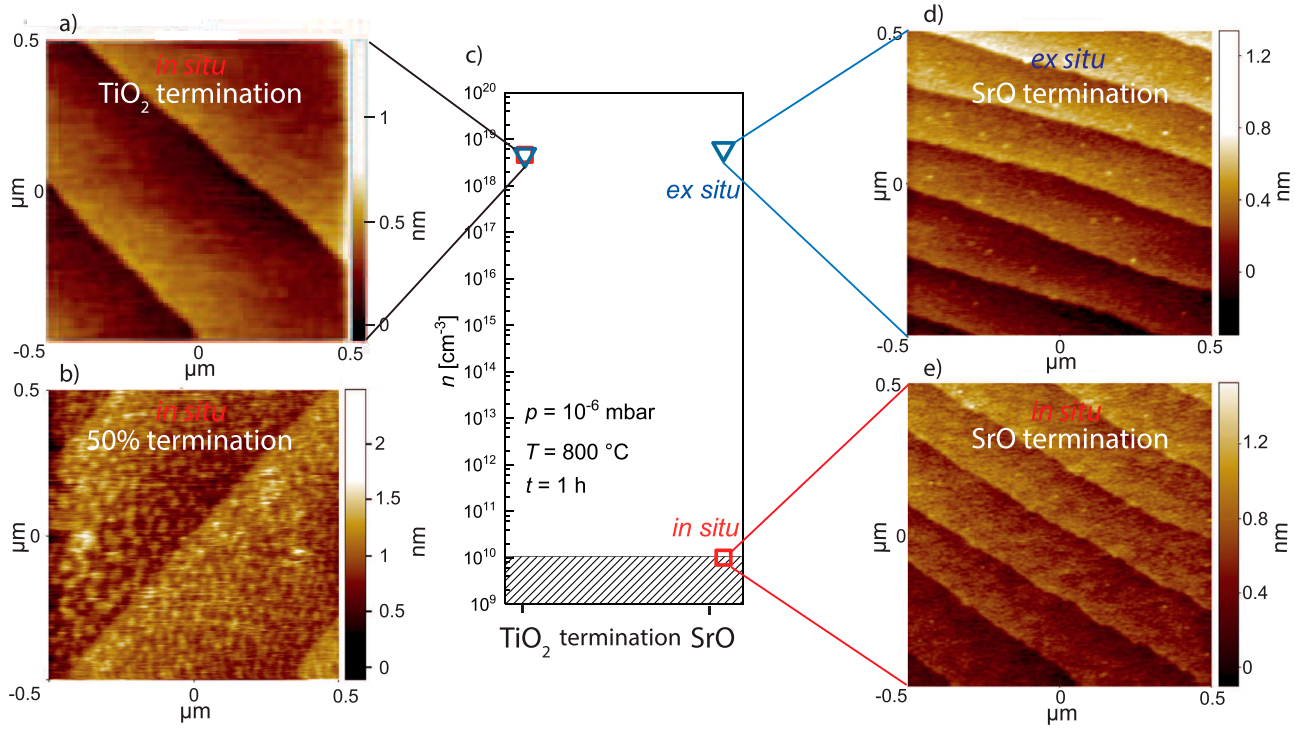


**Figure 1.** (a) Topography of a $TiO_2$ terminated sample and (b) of a 50% terminated sample. (c) Carrier concentration of $TiO_2$ terminated (left) and SrO terminated (right) STO after 1 h of annealing at $10^{-6}$ mbar oxygen pressure and 800°C for an *in situ* sample (red) and a sample stored 60 h in air (blue). (d) The topography of the SrO terminated sample after 60 h of air storage and (e) the topography of a SrO terminated sample measured *in situ* before storage in air. The topography in (d) was measured for the sample presented in (e), after that sample was exposed to air for 60 h.

in high carrier densities independent of the termination (blue triangles). Ambient storage thus affects the reduction of SrO-terminated STO, while the carrier concentration of $TiO_2$-terminated STO remains unchanged.

Concomitant to the reduction behavior of SrO-terminated STO, also the topography changes, when exposed to ambient conditions. Figure 1(e) shows the topography of an *in situ* annealed sample and Figure 1(d) shows the topography of the same sample, but stored 60 h in ambient. While the vicinal surface is atomically flat in the beginning, we can observe features of about 0.2 nm height decorating the unit cell step terraces after ambient storage. The topography of $TiO_2$-terminated STO showed no change after ambient storage. This is a first hint towards the SrO termination being instable, forming Sr containing agglomerates and thus partially opening the SrO termination, revealing parts of a $TiO_2$ termination after ambient storage.

### 3.2. Stability of the SrO termination

We investigated the changes of the surface configuration during exposure to ambient conditions further using *in situ* and *ex situ* XPS in order to investigate the surface chemistry before and after ambient exposure.

The C 1s (Figure 2, top), O 1s (Figure 2, center) and Sr 3d spectra (Figure 2, bottom) were recorded. The C 1s spectrum is of interest as exposure to ambient is expected to give a significant rise to adventitious carbon, which is unavoidable even for *in situ* samples, due to omnipresent C-residuals [57,58]. The O 1s and Sr 3d spectra are of interest to probe chemical changes in the SrO termination layer. The center and right columns show the comparison of the spectra before (*in situ*) and after (*ex situ*) exposure to the ambient for a SrO and a $TiO_2$-terminated sample, respectively.

The fits in the left column of Figure 2 are representatively depicted for the SrO-terminated sample and were obtained in the same manner for the $TiO_2$-terminated sample. The chemical information is gained from these fits. The comparisons in the center and right column elucidate the differences occurring for both terminations before and after exposure to the ambient. The C 1s spectra (Figure 2(a)) are fitted with a carbonate component for the highest binding energy ($E_B$) and a hydrocarbon component ($E_B \approx 286$ eV). The O 1s spectra are fitted using 4 components (Figure 2(b)). The lowest $E_B$ component represents metal oxide bonds in the STO bulk. The highest $E_B$ component represents carbonates [59–61]. Both of the intermediate $E_B$ can be

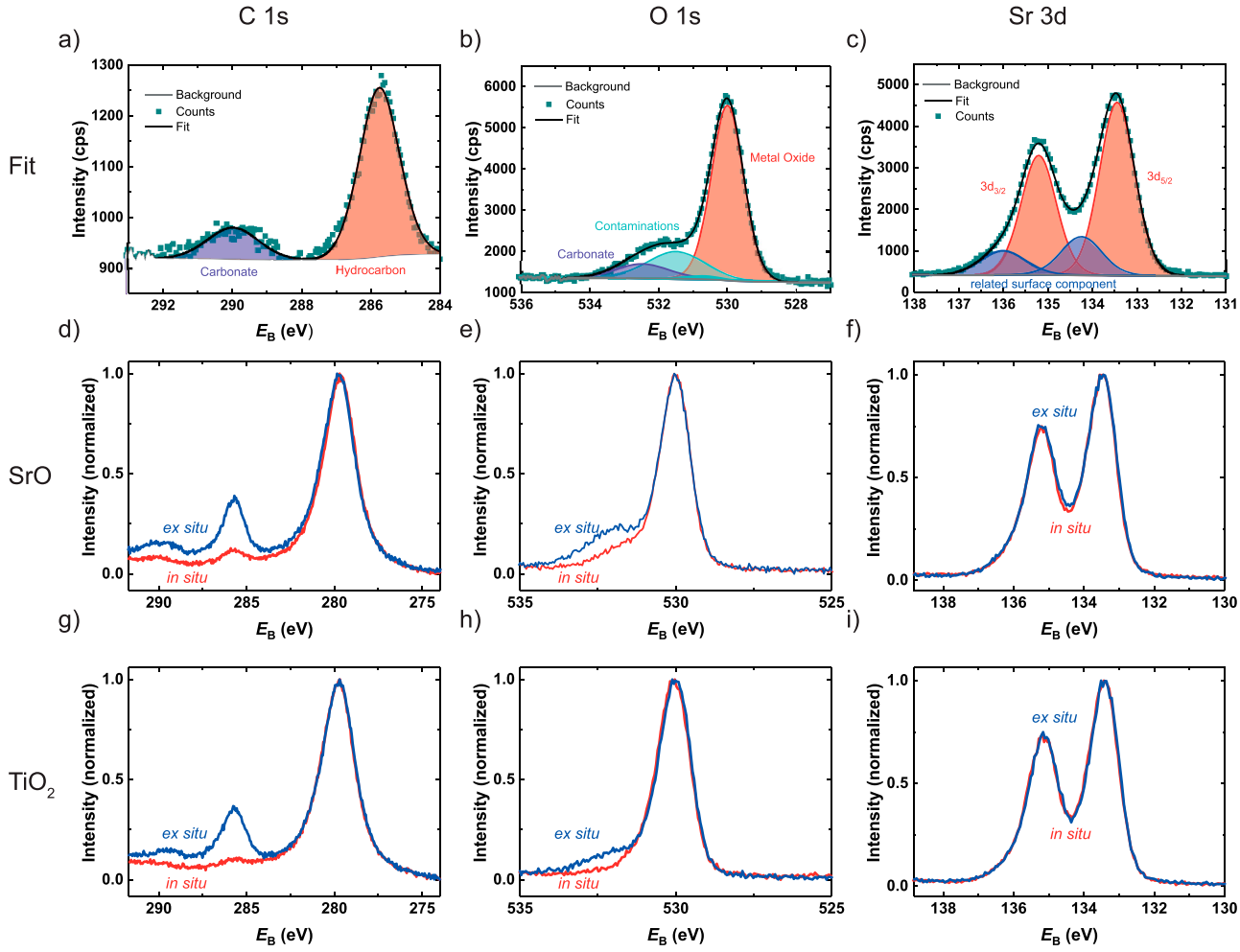


**Figure 2.** Top row shows the fits for (a) the C 1s, (b) O 1s and (c) Sr 3d spectra. The center row shows the comparison of normalized spectra before (*in situ*), blue, and after (*ex situ*), red, ambient exposure for a SrO-terminated sample, the bottom row for a $TiO_2$-terminated sample, respectively. For the C 1s spectrum the change by ambient exposure is more significant for the (d) SrO-terminated sample than the (g) $TiO_2$-terminated sample. The same is observed for the SrO- (e) and $TiO_2$-termination (h) for the O 1s spectrum and the Sr 3d spectrum, (f) and (i), respectively.

ascribed to hydroxides and other non-carbonate contaminations, and are referred to as contaminations peaks. The Sr 3d spectra are composed of a doublet from the STO bulk and a second, surface-related doublet at higher binding energies, as is typically observed for STO (Figure 2(c)) [62].

In order to estimate changes of the surface stoichiometry, we compared the peak areas of the different core-levels. In case of the C 1s spectra, we use the area ratio of the C 1s and Sr $3p_{3/2}$ peaks (Figure 2(d,g)) to obtain a C/Sr ratio. We further use the area of the carbonate and the hydrocarbon peak to obtain a relative carbonate contribution. For the O 1s spectra, we use the areas of the carbonate and the contamination peaks in relation to the metal oxide peak to obtain a relative carbonate contribution and a non-carbonate contamination concentration, respectively. The relative contribution of the Sr related surface component to the Sr 3d signal is obtained from the ratio of the doublet at high binding energy and the doublet from the bulk STO.

These ratios can be found in Table 1 for SrO and $TiO_2$-terminated samples, measured *in situ* and after 60 h of ambient exposure (*ex situ*). After air exposure, the C/Sr ratio increases markedly, to 40%, for both, $TiO_2$- and SrO-termination. For both samples, there is no discernible C 1s carbonate component, when measuring *in situ*. Ambient exposure gives rise to this component, 3.0% for the $TiO_2$-termination and 6.5% for the SrO-termination. The carbonate component is thus markedly the highest for an ambient exposed SrO-termination. Similarly, the O 1s spectra do not exhibit a carbonate component when measuring *in situ*, but after exposure to ambient, this component is 7.5% for the $TiO_2$-termination and 9.5% for the SrO termination. Again

**Table 1.** Ratios obtained from XPS fits for *in situ* and *ex situ* samples, for both $TiO_2$- and SrO-termination, respectively.

| | *In situ* | | *Ex situ* | |
|---|---|---|---|---|
| Termination | $TiO_2$ | SrO | $TiO_2$ | SrO |
| C/Sr ratio (C 1s) | 2.1% | 8.6% | 40% | 40% |
| Carbonate contribution (C 1s) | – | – | 3.0% | 6.5% |
| Contamination concentration (O 1s) | 24% | 21% | 28% | 30% |
| Carbonate contribution (O 1s) | – | – | 7.5% | 9.5% |
| Sr related surface component (Sr 3d) | 18% | 18% | 18% | 21% |

the carbonate component is thus the most pronounced for an ambient exposed SrO-termination. The 3d surface component of the Sr 3d spectra is 18% for the $TiO_2$-termination *in* and *ex situ* and for the *in situ* SrO-termination. Ambient exposure of the SrO-termination increases this spectral weight (21%). This means that the 3d surface component of the Sr 3d spectra only changes after ambient exposing the SrO-terminated STO.

The strong increase of the C/Sr ratio for both terminations is typical for XPS measurements after ambient exposure due to adventitious carbon in the form of carbonate and hydrocarbon [57,58,63,64]. The more pronounced carbonate component of the C 1s and O 1s spectra for the SrO-termination points towards the formation of $SrCO_3$, naturally occurring when SrO reacts with $CO_2$ of the atmosphere [65]. This is also substantiated by the increase of surface component obtained from the Sr 3d spectrum after ambient exposure exclusively for the SrO-termination, as the component could be $SrCO_3$ related. It thus seems that the SrO-termination is instable under ambient conditions due to the formation of $SrCO_3$, eliminating the oxygen vacancy formation inhibiting the effect.

### 3.3. Application to LAO/STO heterostructures

As we have developed a method to tailor the oxygen vacancy incorporation in STO by control of the surface termination under UHV conditions, we next transferred this new method to a thin film system, namely LAO/STO. Since its discovery by Ohtomo *et al.* [38] LAO/STO is by far the most researched oxide 2DEG system.

The formation of a 2DEG results from the evasion of the polar catastrophe by the transfer of half an electron to the $TiO_2$-terminated *n*-type interface, ultimately resulting in a 2DEG [45]. In the same way, one would expect half a hole to be transferred into the p-type interface for a SrO-termination. The potential build-up is, however, in this case compensated by positively charged oxygen vacancies rather than holes [66]. This results in an insulating interface for the SrO-termination [45]. The *n*-type conducting interface was shown to prevail for interfaces with up to 83% SrO-termination, which can be explained by the formation of the 2DEG in the $TiO_2$-terminated areas and percolation paths in between those areas [43,44].

If LAO/STO structures are grown at low oxygen pressures the conduction mechanism changes. We have previously shown that the growth of crystalline LAO at oxygen pressures $\leq 10^{-3}$ mbar results in a shift from 2DEG conductivity to bulk conductivity, when quenching the sample immediately after growth [11,22]. The appearance of bulk conductivity in crystalline LAO/STO can be explained by the incorporation of oxygen vacancies in the STO bulk, which contribute electrons to the conduction band. During its low-pressure growth, LAO sucks oxygen from the underlying STO substrate resulting in the formation of oxygen vacancies in the STO [17]. The shift towards bulk conductivity can easily be identified as it is accompanied by a shift towards much lower resistivity, based on the change of the conductivity mechanism from 2D to 3D [11,14,22,38–43,67–69].

Similar to the bulk conductivity of crystalline LAO/STO grown at low pressures, the 2DEG conductivity of the interface between amorphous LAO and STO single crystals relies on the incorporation of oxygen vacancies into the STO lattice. The main difference is their confinement to the interface in case of amorphous LAO/STO [14,37,70]. Amorphous LAO/STO therefore can be expected to be sensitive to the oxygen vacancy incorporation at the interface. We thus expect to see differences in the conductivity depending on the termination for both, crystalline LAO/STO grown in the bulk-conducting regime (i.e. grown at low pressures) and for amorphous LAO/STO.

Figure 3(a) shows the sheet resistance of crystalline LAO/STO in dependence of temperature obtained for different STO terminations. The sheet resistance of LAO/STO with 0% SrO-termination is about 100 Ω at room temperature and about $10^{-2}$ Ω below 10 K. This corresponds to a dominant metallic bulk conduction of STO, as expected for these growth conditions [22]. An increase of the SrO-termination to 50% results in an increase of the sheet resistance, to about $10^4$ Ω at room temperature and about $10^3$ Ω below 50 K. This is the typical temperature dependency of the sheet resistance for crystalline LAO/STO dominated by 2DEG conductivity [11,14,22,38–43,67–69]. Increasing the SrO-termination further to 100% did, in agreement with observations reported in literature [43,44], result in insulating samples, whose sheet resistance is above the measurement limit ($10^8$ Ω ).

Figure 3(b) shows the sheet resistance of amorphous LAO/STO in dependence of temperature and STO termination. Amorphous LAO/STO with 0% SrO-terminated

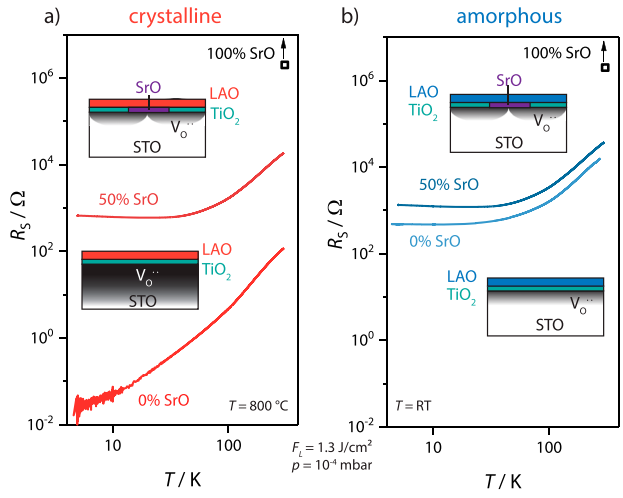


**Figure 3.** Sheet resistance in dependence of temperature of (a) crystalline LAO/STO with different STO terminations and (b) amorphous LAO/STO with different STO terminations. 100% SrO-termination results in insulating behavior for both heterostructures. 50% SrO-termination results in 2DEG conductivity for both, as does 0% SrO termination in the amorphous case. The 0% SrO-terminated crystalline LAO/STO shows metallic conductivity. LAO, both crystalline and amorphous was deposited at $10^{-4}$ mbar. The schematic illustrations are not drawn to scale.

STO has a sheet resistance of about $10^4$ Ω at room temperature and about $10^3$ Ω below 50 K. This is in good agreement with the temperature-dependent resistivity of the 2DEG formed by amorphous LAO/STO, now solely relying on the incorporation of interface oxygen vacancies [14,37,70]. Increasing the SrO-termination of the STO substrate to 50% results in a slight increase of the sheet resistance by a factor of two. A further increase to 100% results, as for the crystalline case, in an insulating sample. Hence, only a negligible amount of oxygen vacancies has formed at the SrO-terminated interface.

Figure 3 shows that we can utilize the termination control of the STO substrate to tailor the sheet resistance in LAO/STO heterostructures. As the sheet resistance of both, crystalline LAO/STO grown in reducing conditions and amorphous LAO/STO, is defined by the oxygen vacancies [11,14,22,37–43,67–70], we have successfully tailored their incorporation. This also explains the shift from bulk dominated to interface dominated conductivity for crystalline LAO, when increasing the SrO-termination to 50% (Figure 3(a)), resulting in a drastic conductivity change over 5 orders of magnitude. The oxygen vacancy incorporation is limited to the remaining $TiO_2$-terminated areas, as shown in the top sketch in Figure 3(a). Considering a homogeneous diffusion of the oxygen vacancies, this limits the conduction to percolation paths at the interface in between these areas. The resulting confined conductivity is comparable to the conductivity of amorphous LAO/STO (Figure 3(b)), which is also dominated by oxygen vacancies confined to the interface, as shown in the according sketches. We can thus in the same way explain the increased resistivity for amorphous LAO/STO.

## 4. Discussion

Considering all the results described above we present a more complete picture of the role of the termination of STO for its oxygen exchange kinetics. Applying conditions known to be reducing for STO single crystals [11,56], we are only able to efficiently incorporate oxygen vacancies into the $TiO_2$-terminated single crystal. The SrO-terminated sample remains insulating. We conclude that the incorporation of oxygen vacancies is inhibited, as other kinetic and thermodynamic factors, e.g. the diffusion coefficient in the bulk, are not affected by termination. We, thus, infer a termination influence on the oxygen exchange kinetics, which we will discuss in more detail in the following.

The surface reaction of the oxygen vacancy incorporation is known to be a multi-step process, which is influenced by several parameters [24,25]. Considering that previous *ab initio* calculations have shown the formation energy of oxygen vacancies to be lower for $TiO_2$-terminated STO as compared to SrO-terminated STO[31,32], it is conceivable that the termination has an influence on one or more steps of the surface reaction.

$$O^{x}_{O,surface} \rightleftharpoons \frac{1}{2}O_2 + V_O^{\bullet\bullet} + 2e^-$$

In particular a high formation energy of oxygen vacancies in SrO-terminated STO could fully depress the oxygen vacancy incorporation at SrO-terminated surfaces. The schematic of this is shown in Figure 4.

Another possible mechanism behind the inhibited oxygen vacancy incorporation is SrO acting as a diffusion barrier for oxygen [71]. However, an increased diffusion barrier was only shown for SrO in a rock salt structure. For SrO in the perovskite structure of STO, the effect was not observed [53]. We thus rule out the explanation of a SrO diffusion barrier, leaving the increased formation energy as a decisive parameter.

The observed behavior, however, changed drastically after SrO-terminated STO was exposed to ambient conditions. Similar vacuum annealing of *ex situ* samples now resulted in high carrier densities independent of termination, indicating that the blocking effect of the SrO termination layer was eliminated by air exposure. This was accompanied by the formation of morphological features,

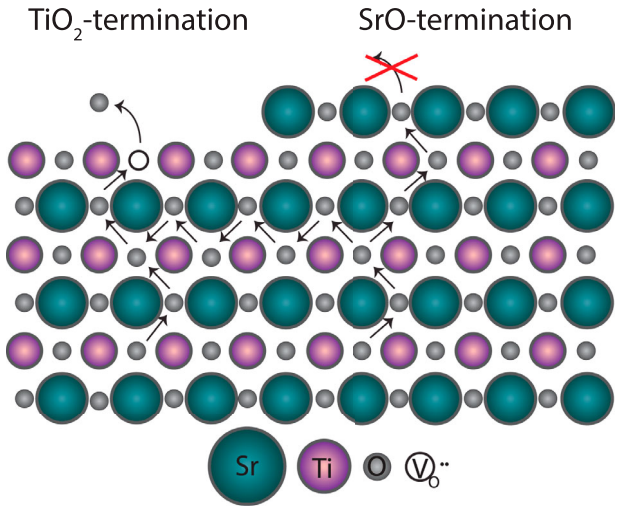


**Figure 4.** Schematic of the oxygen vacancy incorporation at the STO surface for different terminations. Due to the higher formation energy of oxygen vacancies for a SrO-termination, the oxygen vacancy incorporation is suppressed.

indicating a clustering of SrO related particles [53]. Utilizing XPS measurements these particles were identified as $SrCO_3$.

If a SrO-termination inhibits the formation of oxygen vacancies, the formation of $SrCO_3$ can explain the elimination of the effect under ambient conditions. The formation of islands after ambient exposure results in pores in the oxygen blocking SrO-termination layer, revealing the $TiO_2$-terminated STO, which then allows pathways for the incorporation of oxygen vacancies. Moreover, the resulting $SrCO_3$ clusters do not necessarily have a high formation energy for oxygen vacancies.

In principle these results, which were obtained for the (100) crystal orientation, could also be the key to explain similar effects observed for other crystal directions [72,73]. However, the vastly different surface chemistry will surely require future additional calculations and experiments to fully understand the role of the respective terminations.

To profit from our new method to tailor the oxygen vacancy incorporation properties we applied it to the model application of the 2DEG at the LAO/STO heterointerface. Crystalline LAO/STO dominated by bulk conductivity and amorphous LAO/STO both rely on oxygen vacancy incorporation. In the case of crystalline LAO/STO fabricated under reducing conditions we observe a transition from bulk conducting STO (0%) to interface conductivity (50%) and finally to insulating (100%) with an increasing amount of SrO-termination. We explain the drastic change from bulk to interface conductivity with the conductivity of the 50% case being dominated by interface-near oxygen vacancy percolation paths. For amorphous LAO/STO we do as well observe a transition to insulating behavior, when increasing the SrO-termination to 100%.

Considering crystalline LAO/STO this is especially interesting, as it was found that the conductivity in the initial report of 2DEG conductivity by Ohtomo *et al.* [38] was in fact dominated by bulk conductivity, hence by oxygen vacancies [39,40]. Nevertheless, conductivity was only observed for $TiO_2$-terminated STO [38]. This effect could not be explained within the polar catastrophe scenario. With our findings we are able to explain this phenomenon *via* the kinetic inhibition of the oxygen vacancy incorporation for the SrO-terminated sample. They show that in the SrO terminated case no oxygen vacancies are being created during the growth of LAO in reducing conditions at elevated temperatures, corroborating the aspired blocking of oxygen diffusion through the termination layer, and argue against a diffusion limited process.

## 5. Conclusions

With this work, we have provided a novel way to tailor the oxygen vacancy incorporation in STO by controlling its termination. We have demonstrated that a SrO-termination of STO completely inhibits the incorporation of oxygen vacancies for otherwise reducing conditions. By systematically controlling the termination of STO it is thus possible to tailor the areas of oxygen vacancy incorporation. Due to the widespread use of STO as a substrate, this result is highly interesting. A specific application for which we employed this new method is LAO/STO 2DEG heterostructures. By doing so, we were not only able to directly influence the conductivity of these heterostructures but did also improve their understanding. Further applications include, but are not limited to: (i) oxides that require low oxygen pressure growth due to thermodynamic reasons (e.g. $LaVO_3$ [74–76], $EuTiO_3$ [77]), for which film properties would otherwise be masked by oxygen vacancies induced in STO; (ii) metals, which induce the incorporation of oxygen vacancies at the interface [78]. For the LAO/STO system in particular these insights could provide a convenient pathway to intentionally patterning the electron gas for complex electronic applications. This pathway could be further fueled by the recent results providing insights into the different assembly possibilities of sub-monolayer SrO[79].

## Acknowledgments

We further thank R.A. de Souza and M. Müller for helpful discussions.

## Disclosure statement

No potential conflict of interest was reported by the authors.

## Funding

We acknowledge funding from the W2/W3 program of the Helmholtz Association. The research has furthermore been supported by the Deutsche Forschungsgemeinschaft (SFB 917 'Nanoswitches'). FG and MR thank the DFG GU/1604. CB has received funding from the European Union's Horizon 2020 research and innovation program under the Marie Sklodowska-Curie grant agreement no. 796142.

## ORCID

*Felix V. E. Hensling* http://orcid.org/0000-0003-3852-7214

## References

[1] Rao C. Transition metal oxides. Annu Rev Phys Chem. 1989;40(40):291–326.
[2] Christen HM, Eres G. Recent advances in pulsed-laser deposition of complex oxides. J Phys Condens Matter. 2008;20(26):264005.
[3] Waser R, Dittmann R, Staikov C, et al. Redox-based resistive switching memories nanoionic mechanisms, prospects, and challenges. Adv Mater. 2009;21(25–26): 2632–2663.
[4] Kawasaki S, Takahashi R, Yamamoto T, et al. Photoelectrochemical water splitting enhanced by self-assembled metal nanopillars embedded in an oxide semiconductor photoelectrode. Nat Commun. 2016;7(May):1–6. Available from: http://dx.doi.org/10.1038/ncomms11818.
[5] Brooks CM, Wilson RB, Schäfer A. Tuning thermal conductivity in homoepitaxial $SrTiO_3$ films via defects. Appl Phys Lett. 2015;107(5):162905.
[6] Breckenfeld E, Wilson R, Karthik J, et al. Effect of growth induced (non)stoichiometry on the structure, dielectric response, and thermal conductivity of $SrTiO_3$ thin films. Chem Mater. 2012;24(2):331–337.
[7] Tan H, Zhao Z, Zhu WB, et al. Oxygen vacancy enhanced photocatalytic activity of pervoskite $SrTiO_3$. ACS Appl Mater Interfaces. 2014;6(21):19184–19190.
[8] Mueller DN, MacHala ML, Bluhm H, et al. Redox activity of surface oxygen anions in oxygen-deficient perovskite oxides during electrochemical reactions. Nat Commun. 2015;6:1–8. Available from: http://dx.doi.org/10.1038/ncomms7097.
[9] Janousch M, Meijer GI, Staub U, et al. Role of oxygen vacancies in cr-doped $SrTiO_3$ for resistance-change memory. Adv Mater. 2007;19(17):2232–2235.
[10] Szot K, Speier W, Bihlmayer G, et al. Switching the electrical resistance of individual dislocations in single-crystalline $SrTiO_3$. Materials¡/DIFdel¿Nat Mater. 2006;5 (4):312–320.
[11] Hensling FVE, Xu C, Gunkel F. Unraveling the enhanced oxygen vacancy formation in complex oxides during annealing and growth. Sci Rep. 2017;7(November 2016):39953.
[12] Hensling FVE, Keeble DJ, Zhu J, et al. UV radiation enhanced oxygen vacancy formation caused by the PLD plasma plume. Sci Rep. 2018;8(1):8846.
[13] Lee HN, Seo SSA, Choi WS, et al. Growth control of oxygen stoichiometry in homoepitaxial $SrTiO_3$ films by pulsed laser epitaxy in high vacuum. Sci Rep. 2016;6(October 2015):19941.
[14] Sambri A, Cristensen DV, Trier F, et al. Plasma plume effects on the conductivity of amorphous-$LaAlO_3/SrTiO_3$ interfaces grown by pulsed laser deposition in $O_3$ and Ar. Appl Phys Lett. 2012;100(23):231605.
[15] Scullin ML, Ravichandran J, Yu C, et al. Pulsed laser deposition-induced reduction of $SrTiO_3$ crystals. Acta Mater. 2010;58(2):457–463.
[16] Chen F, Lu H, Chen Z, et al. Optical real-time monitoring of the laser molecular-beam epitaxial growth of perovskite oxide thin films by an oblique-incidence reflectance-difference technique: erratum. J Opt Soc Am B. 2002;19(7):1218.
[17] Schneider CW, Esposito M, Marozau I, et al. The origin of oxygen in oxide thin films: role of the substrate. Appl Phys Lett. 2010;97(19):95–98.
[18] Gunkel F, Hoffmann-Eifert S, Dittmann R, et al. High temperature conductance characteristics of $LaAlO_3/SrTiO_3$-heterostructures under equilibrium oxygen atmospheres. Appl Phys Lett. 2010;97(1):2–4.
[19] Moos R, Menesklou W, Hardtl KH. Hall-mobility of undoped N-type conducting strontium-titanate single-crystals between 19-K and 1373-K. Appl Phys a – Mater Sci Process. 1995;61(4):389–395.
[20] Moos R, Hardtl KH. Defect chemistry of donor-doped and undoped strontium titanate ceramics between 1000 degrees and 1400 degrees C. J Am Ceram Soc. 1997;80(10): 2549–2562.
[21] De Souza RA, Metlenko V, Park D, et al. Behavior of oxygen vacancies in single-crystal $SrTiO_3$: equilibrium distribution and diffusion kinetics. Phys Rev B Condens Matter Mater Phys. 2012;85(17):1–11.
[22] Xu C, Bäumer C, Heinen RA, et al. Disentanglement of growth dynamic and thermodynamic effects in $LaAlO_3/SrTiO_3$ heterostructures. Sci Rep. 2016;6(1): 22410. Available from: http://www.nature.com/articles/srep22410.
[23] Merkle R, Souza RAD, Maier J. Optically tuning the rate of stoichiometry changes: surface-controlled oxygen incorporation into oxides under UV irradiation. Angew Chem (Int Ed Engl). 2001;4(11):2126–2129.
[24] Merkle R, Maier J. Oxygen incorporation into Fe-doped $SrTiO_3$: mechanistic interpretation of the surface reaction. Phys Chem Chem Phys. 2002;4(17):4140–4148.
[25] Merkle R, Maier J. How is oxygen incorporated into oxides? A comprehensive kinetic study of a simple solid-state reaction with $SrTiO_3$ as a model material. Angew Chem – Int Ed. 2008;47(21):3874–3894.
[26] Leonhardt M, De Souza RA, Claus J, et al. Surface kinetics of oxygen incorporation into $SrTiO_3$. J Electrochem Soc. 2002;149(2):J19–J26.
[27] Walch G, Rotter B, Brunauer GC, et al. A solid oxide photoelectrochemical cell with UV light-driven oxygen storage in mixed conducting electrodes. J Mater Chem A. 2017;5(4):1637–1649.

[28] Tascón JM, Tejuca LG. Adsorption of $CO_3$ on the perovskite-type oxide $LaCoO_3$. J Chem Soc Faraday Trans. 1981;1(77):591–602.
[29] Huang K, Chu X, Yuan L, et al. Engineering the surface of perovskite $La_{0.5}Sr_{0.5}MnO_3$ for catalytic activity of CO oxidation. Chem Commun. 2014;50(65):9200–9203.
[30] Maiti D, Daza YA, Yung MM, et al. Oxygen vacancy formation characteristics in the bulk and across different surface terminations of $La_{(1-x)}Sr_xFe_{(1-y)}Co_yO_{(3-d)}$ perovskite oxides for $CO_2$ conversion. J Mater Chem A. 2016;4(14):5137–5148.
[31] Alexandrov VE, Kotomin Ea, Maier J, et al. First-principles study of bulk and surface oxygen vacancies in $SrTiO_3$ crystal. Eur Phys J B. 2009;72(1):53–57.
[32] Silva AR, Dalpian GM. Oxygen vacancies at the surface of $SrTiO_3$ thin films. J Appl Phys. 2014;115(3):033710.
[33] Kawasaki M, Takahashi K, Maeda T, et al. Atomic control of the $SrTiO_3$ crystal surface. Science. 1994;266(5190):1540–1542.
[34] Koster G, Rijnders G, Blank DHA, et al. Surface morphology determined by (0 0 1) single-crystal $SrTiO_3$ termination. Physica C. 2000;339:215–230.
[35] Zheng B, Binggeli N. Influence of the interface atomic structure on the magnetic and electronic properties of $La_{2/3}Sr_{1/3}MnO_3/SrTiO_3$(001) heterojunctions. Phys Rev B. 2010;82(24):245311.
[36] Rijnders G, Currás S, Huijben M, et al. Influence of substrate-film interface engineering on the superconducting properties of $YBa_2Cu_3O_7$-$\delta$. Appl Phys Lett. 2004;84(7):1150–1152.
[37] Chen Y, Pryds N, Kleibeuker JE, et al. Metallic and insulating interfaces of amorphous $SrTiO_3$-based oxide heterostructures. Nano Lett. 2011;11(9):3774–3778.
[38] Ohtomo A, Hwang HY. A high-mobility electron gas at the LAO/STO heterointerface. Nature. 2004;427(6973):423–426.
[39] Breckenfeld E, Bronn N, Karthik J, et al. Effect of growth induced (non)stoichiometry on interfacial conductance in $LaAlO_3/SrTiO_3$. Phys Rev Lett. 2013;110(19):1–6.
[40] Herranz G, Basletić M, Bibes M. High mobility in $LaAlO_3/SrTiO_3$ heterostructures: origin, dimensionality, and perspectives. Phys Rev Lett. 2007;98(21):216803.
[41] Kalabukhov A, Gunnarsson R, Boerjesson J, et al. Effect of oxygen vacancies in the $SrTiO_3$ substrate on the electrical properties of the $LaAlO_3$ $SrTiO_3$ interface. Phys Rev B Condens Matter Mater Phys. 2007;75(12):2–5.
[42] Cancellieri C, Reyren N, Gariglio S, et al. Influence of the growth conditions on the $LaAIO_3/SrTiO_3$ interface electronic properties. EPL (Europhys Lett). 2010;91(1):17004.
[43] Huijben M, Brinkman A, Koster G, et al. Structure–property relation of $SrTiO_3/LaAlO_3$ interfaces. Adv Mater. 2009;21(17):1665–1677.
[44] Nishimura J, Ohtomo A, Ohkubo A. Controlled carrier generation at a polarity-discontinued perovskite heterointerface. Jpn J Appl Phys Part 2 Lett. 2004;43(8 A):L1032.
[45] Nakagawa N, Hwang HY, Muller DA. Why some interfaces cannot be sharp. Nat Mater. 2006;5(3):204–209.
[46] Woltmann C, Harada T, Boschker H, et al. Field-effect transistors with submicrometer gate lengths fabricated from $LaAlO_3$-$SrTiO_3$-based heterostructures. Phys Rev Appl. 2015;4(6):1–6.
[47] Goswami S, Mulazimoglu E, Vandersypen LM, et al. Nanoscale electrostatic control of oxide interfaces. Nano Lett. 2015;15(4):2627–2632.
[48] Liu Q, Dong L, Liu Y, et al. Frequency response of $LaAlO_3/SrTiO_3$ all-oxide field-effect transistors. Solid State Electron. 2012;76:1–4.
[49] Hosoda M, Hikita Y, Hwang HY, et al. Transistor operation and mobility enhancement in top-gated $LaAlO_3/SrTiO_3$ heterostructures. Appl Phys Lett. 2013;103(10):4–7.
[50] Eerkes PD, Van Der Wiel WG, Hilgenkamp H. Modulation of conductance and superconductivity by top-gating in $LaAlO_3/SrTiO_3$ 2-dimensional electron systems. Appl Phys Lett. 2013;103(20):2–6.
[51] Liu W, Gariglio S, Fête A, et al. Magneto-transport study of top- and back-gated $LaAlO_3/SrTiO_3$ heterostructures. APL Mater. 2015;3(6):062805.
[52] Hurand S, Jouan A, Feuillet-Palma C, et al. Field-effect control of superconductivity and Rashba spin–orbit coupling in top-gated $LaAlO_3/SrTiO_3$ devices. Sci Rep. 2015;5(February):1–9. Available from: http://dx.doi.org/10.1038/srep12751.
[53] Hensling F, Heisig T, Raab N. Tailoring the switching performance of resistive switching $SrTiO_3$ devices by SrO interface engineering. Solid State Ionics. 2018;325(July):247–250.
[54] Nie YF, Zhu Y, Lee CH, et al. Atomically precise interfaces from non-stoichiometric deposition. Nat Commun. 2014;5(1):4530.
[55] Baeumer C, Xu C, Gunkel F, et al. Surface termination conversion during $SrTiO_3$ thin film growth revealed by X-ray photoelectron spectroscopy. Sci Rep. 2015;5(1):11829. Available from: http://www.nature.com/articles/srep11829.
[56] Frederikse HPR, Thurber WR, Hosler WR. Electronic transport in strontium titanate. Phys Rev. 1964;134(2A):2–5.
[57] Barr TL, Seal S. Nature of the use of adventitious carbon as a binding energy standard. J Vacuum Sci Tech A Vacuum Surf Films. 1995;13(3):1239–1246.
[58] Swift P. Adventitious carbon – the panacea for energy referencing? Surf Interface Anal. 1982;4(2):47–51.
[59] Shchukarev AV, Korolkov DV. XPS study of group IA carbonates. Central Eur J Chem. 2004;2(2):347–362.
[60] Lam K, Gao Y, Wang J, et al. $H_2O_2$ Treated $La_{0.8}Sr_{0.2}CoO_3$-$\delta$ as an efficient catalyst for oxygen evolution reaction. Electrochim Acta. 2017;244(2018):139–145.
[61] Crumlin EJ, Mutoro E, Liu Z, et al. Surface strontium enrichment on highly active perovskites for oxygen electrocatalysis in solid oxide fuel cells. Energy Environ Sci. 2012;5(3):6081.
[62] Szot K, Speier W, Breuer U, et al. Formation of microcrystals on the (100) surface of $SrTiO_3$ at elevated temperatures. Surf Sci. 2000;460:112.
[63] Piao H, McIntyre NS. Adventitious carbon growth on aluminium and gold-aluminium alloy surfaces. Surf Interface Anal. 2002;33(7):591–594.
[64] Miller DJ, Biesinger MC, McIntyre NS. Interactions of $CO_2$ and CO at fractional atmosphere pressures

with iron and iron oxide surfaces: one possible mechanism for surface contamination? Surf Interface Anal. 2002;33(4):299–305.
[65] Ropp R. The alkaline earths as metals. In: Encyclopedia of the alkaline earth compounds. 1st ed. Chapter 1. Amsterdam: Elsevier; 2013. p. 1–23.
[66] Lee H, Campbell N, Lee J, et al. Direct observation of a two-dimensional hole gas at oxide interfaces. Nat Mater. 2018;17(3):231–236.
[67] Amoruso S, Aruta C, Bruzzese R, et al. Substrate heating influence on the deposition rate of oxides during pulsed laser deposition in ambient gas. Appl Phys Lett. 2011;98(10):101501–3.
[68] Amoruso S, Aruta C, Aurino P, et al. Oxygen background gas influence on pulsed laser deposition process of $LaAlO_3$ and $LaGaO_3$. Appl Surf Sci. 2012;258:9116–9122.
[69] Hwang HY, Ohtomo A, Nakagawa N, et al. High-mobility electrons in $SrTiO_3$ heterostructures. Phys E: Low-Dimens Syst Nanostruct. 2004;22(1–3):712–716.
[70] Trier F, Amoruso S, Christensen DV, et al. Controlling the conductivity of amorphous $LaAlO_3/SrTiO_3$ interfaces by in-situ application of an electric field during fabrication. Appl Phys Lett. 2013;103(3):1–6.
[71] Baeumer C, Schmitz C, Ramadan AHH, et al. Spectromicroscopic insights for rational design of redox-based memristive devices. Nat Commun. 2015;6:8610.
[72] Zhu Y, Salvador PA, Rohrer GS. Controlling the relative areas of photocathodic and photoanodic terraces on the $SrTiO_3$(111) surface. Chem Mater. 2016;28(14):5155–5162.
[73] Zhu Y, Salvador PA, Rohrer GS. Controlling the termination and photochemical reactivity of the $SrTiO_3$ (110) surface. Phys Chem Chem Phys. 2017;19(11):7910–7918.
[74] Hotta Y, Susaki T, Hwang HY. Polar discontinuity doping of the $LaVO_3/SrTiO_3$ interface. Phys Rev Lett. 2007;99(23):3–6.
[75] He C, Sanders TD, Gray MT, et al. Metal-insulator transitions in epitaxial $LaVO_3$ and $LaTiO_3$ films. Phys Rev B Condens Matter Mater Phys. 2012;86(8):1–4.
[76] Vrejoiu I, Himcinschi C, Jin L, et al. Probing orbital ordering in $LaVO_3$ epitaxial films by Raman scattering. APL Mater. 2016;4(4):046103–10.
[77] Shkabko A, Xu C, Meuffels P, et al. Tuning cationic composition of La:$EuTiO_3$-$\delta$ films. APL Mater. 2013;1(5):0–9.
[78] Santander-Syro AF, Copie O, Kondo T, et al. Two-dimensional electron gas with universal subbands at the surface of $SrTiO_3$. Nature. 2011;469(7329):189–194.
[79] Gagnidze T, Ma H, Cancellieri C, et al. Structural properties of ultrathin SrO film deposited on $SrTiO_3$. Sci Technol Adv Mater. 2019;20(1):456–463.